Mouse models of *MYH9*-related disease: mutations in nonmuscle myosin II-A

Yingfan Zhang,[1] Mary Anne Conti,[1] Daniela Malide,[1] Fan Dong,[2] Aibing Wang,[1] Yelena A. Shmist,[1] Chengyu Liu,[1] Patricia Zerfas,[3] Mathew P. Daniels,[1] Chi-Chao Chan,[4] Elliot Kozin,[5] Bechara Kachar,[5] Michael J. Kelley,[2,6] Jeffrey B. Kopp,[7] and Robert S. Adelstein[1]

[1]National Heart, Lung, and Blood Institute, National Institutes of Health (NIH), Bethesda, MD; [2]Department of Medicine, Duke University Medical Center, Durham, NC; [3]Office of Research Services, Division of Veterinary Resources, [4]National Eye Institute, and [5]National Institute on Deafness and Other Communication Disorders, NIH, Bethesda, MD; [6]Medical Service, Durham Veterans Affairs Medical Center, Durham, NC; and [7]National Institute of Diabetes and Digestive and Kidney Diseases, NIH, Bethesda, MD

We have generated 3 mouse lines, each with a different mutation in the nonmuscle myosin II-A gene, *Myh9* (R702C, D1424N, and E1841K). Each line develops *MYH9*-related disease similar to that found in human patients. R702C mutant human cDNA fused with green fluorescent protein was introduced into the first coding exon of *Myh9*, and D1424N and E1841K mutations were introduced directly into the corresponding exons. Homozygous R702C mice die at embryonic day 10.5-11.5, whereas homozygous D1424N and E1841K mice are viable. All heterozygous and homozygous mutant mice show macrothrombocytopenia with prolonged bleeding times, a defect in clot retraction, and increased extramedullary megakaryocytes. Studies of cultured megakaryocytes and live-cell imaging of megakaryocytes in the BM show that heterozygous R702C megakaryocytes form fewer and shorter proplatelets with less branching and larger buds. The results indicate that disrupted proplatelet formation contributes to the macrothrombocytopenia in mice and most probably in humans. We also observed premature cataract formation, kidney abnormalities, including albuminuria, focal segmental glomerulosclerosis and progressive kidney disease, and mild hearing loss. Our results show that heterozygous mice with mutations in the myosin motor or filament-forming domain manifest similar hematologic, eye, and kidney phenotypes to humans with *MYH9*-related disease. (*Blood*. 2012;119(1): 238-250)

Introduction

Point mutations in *MYH9*, the gene encoding nonmuscle myosin heavy chain II-A (NMHCII-A), underlie autosomal dominant syndromes in humans (incidence, ~ 1 in 500 000).[1-3] The human abnormalities manifest as macrothrombocytopenia, granulocyte inclusions, progressive proteinuric renal disease, cataracts, and sensorineural deafness. Most patients have a mild bleeding tendency. Patients may develop early or late onset deafness, cataracts, and progressive glomerulosclerosis, leading to kidney failure. These syndromes, now referred to as *MYH9*-related diseases (*MYH9*-RDs), were formerly called May-Hegglin, Fechtner, Sebastian, and Epstein syndromes.[1,4]

Each nonmuscle myosin II (NMII) molecule is composed of a pair of heavy chains (M_r = 230 000) and 2 pairs of light chains (M_r 20 000 and 17 000). NMII has 3 paralogs, NMII-A, NMII-Bm and NMII-C, whose heavy chains are encoded by 3 different genes *MYH9*, *MYH10*, and *MYH14*, respectively, located on 3 different human chromosomes (22, 17, and 19). NMIIs are ubiquitously expressed but differ with respect to localization and expression levels in cells, although they may also overlap with each other.[5] The NMII protein is markedly asymmetric with a globular-shaped motor domain at one end containing the enzymatic activity that hydrolyzes MgATP to convert chemical energy into the mechanical translocation of actin filaments. The other end of the molecule is a long α-helical rod that dimerizes the 2 heavy chains and participates in the formation of bipolar filaments, composed of ~ 28 molecules,[6] which are required for most NMII functions. As a motor protein that is able to form bipolar filaments that can cross-link and exert force on actin filaments, NMII is involved in a variety of cellular processes, including cell adhesion, migration, cytokinesis, and shape maintenance.[7]

To date > 40 different disease-related mutations in human patients have been found in *MYH9* exons. Most are point mutations and cluster in limited regions of the gene.[8] Although NMII-A is widely distributed in a variety of tissues, the mutations in human patients affect only a limited number of tissues. The blood syndrome involves platelets and granulocytes, which only express NMII-A.[9] Not all patients have complications in the eye lens, inner ear, and kidney, indicating that other NMII paralogs (ie, NMII-B and NMII-C) or proteins other than NMII may function to compensate for the mutant NMII-A.

Here, we report the generation and characterization of 3 different mutant *Myh9* mouse lines. The knock-in mutations are Arg702Cys (R702C), Asp1424Asn (D1424N), and Glu1841Lys (E1841K). These 3 mutations are the most frequent mutations found in human patients.[10] The R702C mutation is located in the motor domain of NMII-A, and an in vitro study shows that R702C decreases the NMII-A actin-activated MgATPase activity.[11] The D1424N and E1841K mutations are located in the rod domain and may affect NMII-A filament formation.[12] Our data show that the mutant mice recapitulate defects found in humans as heterozygous and in 2 cases (D1424N and E1841K) as homozygous mice.

Submitted June 3, 2011; accepted August 29, 2011. Prepublished online as *Blood* First Edition paper, September 8, 2011; DOI 10.1182/blood-2011-06-358853.

The online version of this article contains a data supplement.

The publication costs of this article were defrayed in part by page charge payment. Therefore, and solely to indicate this fact, this article is hereby marked "advertisement" in accordance with 18 USC section 1734.

Methods

Generation of transgenic mice

All mouse procedures were performed with approval from the National Heart, Lung, and Blood Institute Animal Care and Use Committee and Duke University Medical School Institutional Animal Care and Use Committee. To generate the knock-in NMHCII-A R702C mutant construct for homologous recombination, DNA fragments flanking exon2, the first coding exon of the mouse *Myh9* gene, were amplified from a 129S6/SvEv genomic BAC clone harboring the complete *Myh9* locus.[13] The 5′ arm, ~ 4-kb immediately upstream of the initiating ATG codon in exon2, is followed by a cDNA cassette encoding enhanced green fluorescent protein (eGFP)–human NMHCII-A with the R702C mutation, SV40 polyA, a loxP-flanked PGK-Neo^r cassette and the ~ 2-kb genomic sequence 3′ of the ATG codon (supplemental Figure 1A, available on the *Blood* Web site; see the Supplemental Materials link at the top of the online article). To generate the knock-in NMHCII-A D1424N mutant construct, a 3.1-kb DNA fragment upstream of a *Kpn*I site in the intron between exon 31 and exon 32 was amplified from the same 129S6/SvEv genomic BAC clone, and the D1424N mutation was introduced into exon 31. The targeting construct consists of a 3.1-kb 5′ arm containing the D1424N mutation, followed by a loxP-flanked PGK-Neo^r cassette, and the 3.9-kb 3′ arm (supplemental Figure 1B). To generate the knock-in NMHCII-A E1841K mutant construct, a 1.1-kb DNA fragment containing exon 39 and exon 40 was amplified from BAC clone 144L21, and the E1841K mutation was introduced into exon 39 by PCR. The targeting construct contains a 13-kb 5′ arm, followed by a loxP-flanked Neo^r cassette, and the 1.1-kb 3′ arm containing exons 39 and 40 (supplemental Figure 1C). The E1841K mutant mouse was generated at Duke University Medical Center and characterized at the National Institutes of Health where the R702C and D1424N mice were generated and characterized. To generate a wild-type control mouse with GFP-tagged to the N-terminus of NMHCII-A, the eGFP sequence was inserted 5′ of the initiating ATG codon in exon 2. The 4-kb 5′ arm immediately upstream of the ATG is followed by the eGFP-tagged exon 2 plus 160-bp DNA sequence immediately 3′ of exon 2, a loxP-flanked PGK-Neo^r cassette and the 2-kb 3′ arm (supplemental Figure 1D). Nucleotide sequences of the cloned DNA fragments and the mutations were confirmed by sequencing. The mutant nucleotide sequences in genomic DNA of the knock-in mice were also confirmed by sequencing. Genotyping was performed by PCR (supplemental Table 1).

Generation of NMII-Aflox mice (deposited with MMRRC #32096) has been described.[14] To delete NMII-A specifically in the podocytes, mice were crossed to podocin-cre mice[15] generously provided by the Quaggin laboratory (Mt Sinai Hospital, Toronto). CMV-cre mice are from The Jackson Laboratory. Mice were bred by sibling mating except the A^{E1841K} strain that was back-crossed for 6 generations to C57BL/6.

Confocal and 2-photon microscopy

GFP-NMII was visualized by confocal and multiphoton microscopy in intact tissues without fixation or sectioning. BM was examined at multiple locations: through the calvaria without sectioning, inside the sternum by opening the bone,[16] and inside long bones (femur) through a sagittal section exposing the marrow underneath.

BM whole-mount samples were imaged with a Leica SP5-AOBS confocal and multiphoton system (Leica Microsystems). In confocal mode 488-nm Argon, 561-nm, and 633-nm lasers were used to image GFP, Rhodamine RX, and APC, respectively. In 2-photon mode a pulsed femtosecond Ti:Sapphire laser (Chameleon Vision II) from Coherent, tunable for excitation from 680 to 1080 nm with group velocity dispersion precompensation and imaging on external non-descanned detectors was used. Two-photon excitation at 920 nm of GFP fluorescence was combined with second harmonic generation (SHG) microscopy of bone collagen structure. All images (Figures 5A-B,D and 6B) were taken with a HCX-IRAPO-L25 × NA 0.95 water immersion dipping objective (WD = 2.2mm). For time-lapse imaging, freshly excised BM samples were placed cut-face down onto 35-mm coverglass culture dishes (MatTek Corporation), in 50-100 μL of DMEM, 10% FBS containing 20mM HEPES at 37°C, and 2-photon excitation (920 nm) was performed with a Leica resonant scanner (8000 Hz/s) taking z-stacks (~ 150 μm) at 10-second intervals for ≤ 2 hours. In some experiments time-lapse was performed on a Zeiss 510 META confocal system where z-stacks were imaged every 10 minutes for ≤ 8-10 hours (Plan Apo 40× NA1.3 oil immersion objective). For 3D volume-rendering series of x-y-z images (typically 680 × 680 μm^2) x-y size were collected along the z-axis at intervals of 1-4 μm to depths of ~ 150-250 μm throughout the BM. In some circumstances, large regions were scanned with the tile function of the software to generate stitched volumes comprising ~ 2.5 × 1.2 mm^2 (x-y) and 250 μm (z). For images in Figures 4A-B,E, 5C,E, 6C and 7C, a Zeiss 510 META confocal system was used with a 20× objective in air.

Volume data were used to create 3D renderings of megakaryocyte (MK) and platelet distributions inside BM, and time-lapse data were exported as 3D-videos using Imaris 7.1 and 7.2 software (Bitplane).

Electron microscopy

For transmission electron microscopy (EM), mouse kidney and BM were fixed and processed as described,[17] except that, after osmium tetroxide, tissues were fixed with 1% uranyl acetate for 1 hour. The grids were viewed in the JEM-1200 EXII electron microscope (JEOL Ltd) at 80kV and images were recorded on the XR611M, mid mounted, 10.5Mpixel, CCD camera (Advanced Microscopy Techniques Corp), for Figures 3Diii and 7D, Eiii-iv.

For scanning EM, kidneys were fixed in 2.5% glutaraldehyde, 1% paraformaldehyde, 0.12M sodium cacodylate buffer, pH 7.4, for 1 hour at room temperature and overnight at 4°. The cortex was cut into 1-mm^3 pieces, washed in cacodylate buffer, postfixed in 1% OsO4 in cacodylate buffer for 1.5 or 2.5 hours, washed in H_2O, dehydrated in ethanol, and critical point dried. Dried pieces of cortex were mounted on SEM stubs with carbon adhesive, fractured with a single-edged razor, and sputter-coated with 10 nm of gold. The fracture surfaces were examined with a Hitachi S3400-N1 scanning electron microscope.

Light microscopy

Images in Figures 2A, 3A, 3Dii, and 6A were acquired with a Nikon 100× oil objective at room temperature using a Zeiss AxioCam HRc camera. Images in Figures 3C, 3Di, and 7A were acquired with an Olympus BX40 40× air objective at room temperature using a SpotFlex camera.

Results

Generation of 3 mutant NMII-A and GFP-NMII-A mouse lines

To generate mouse models of *MYH9*-RDs and to investigate the pathologic mechanism of the associated syndromes, 3 different human disease-associated mutations, R702C, D1424N, and E1841K, were separately introduced into the mouse *Myh9* gene. In addition to the prevalence of these 3 mutations, they were also chosen because they occur in 2 different domains of the NMII molecule and affect different properties of NMII. As shown in supplemental Figure 1, the R702C-mutated human NMHCII-A cDNA fused to GFP was targeted into exon 2, the first coding exon of *Myh9* just 5′ of the initiating ATG codon. (The human NMHCII-A amino acid sequence is 97% identical to the mouse NMHCII-A.) This simultaneously ablates expression of the endogenous gene and permits GFP-tagged human NMHCII-A with the R702C mutation to be expressed under control of the endogenous mouse *Myh9* promoter. GFP expression allowed visualization of the mutant NMII during platelet development as well as in other organs expressing NMII-A. The D1424N and E1841K mutations were introduced independently into constructs containing exon 31 or exon 39, respectively, with the use of PCR (supplemental Figure 1B-C). The mutant

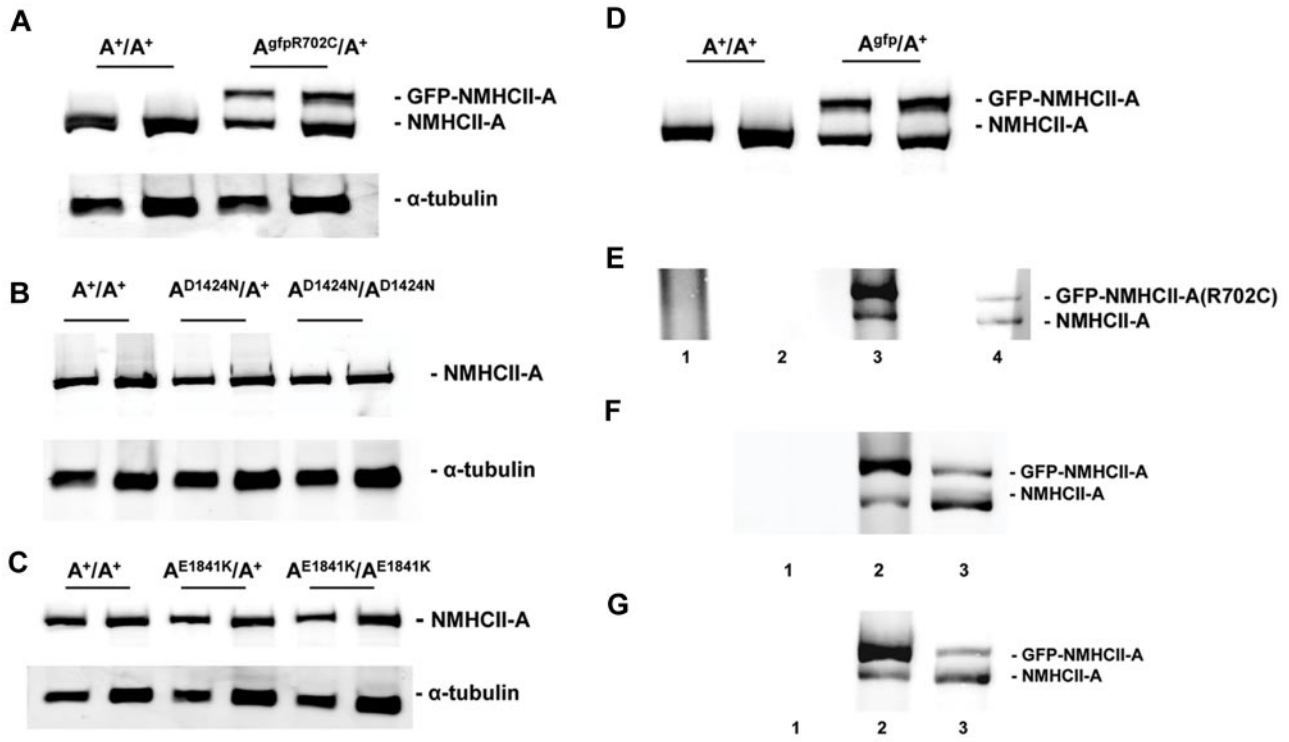

Figure 1. Immunoblot analysis of NMHCII-A expression levels in adult mouse lung tissue. (A) Analysis of NMHCII-A expression from extracts of A^+/A^+ and $A^{gfpR702C}/A^+$ mouse lung. Note that mutant GFP–NMHCII-A protein migrates more slowly than endogenous NMHCII-A. Mutant GFP–NMHCII-A and endogenous NMHCII-A were detected with anti–NMHCII-A. In the $A^{gfpR702C}/A^+$ lung tissue, the expression level of the GFP–NMHCII-A R702C is ~ 80% of the endogenous NMHCII-A. There are 2 different loadings for each sample. (B) Immunoblot analysis of NMHCII-A expression in A^+/A^+, A^{D1424N}/A^+, and A^{D1424N}/A^{D1424N} tissue shows that approximately the same amount of NMHCII-A protein, normalized to tubulin, is expressed in the A^+/A^+, A^{D1424N}/A^+, and A^{D1424N}/A^{D1424N} mouse lung. (C) Immunoblot analysis of NMHCII-A expression in A^+/A^+, A^{E1841K}/A^+, and A^{E1841K}/A^{E1841K} lung shows that similar amounts of NMHCII-A are expressed normalized to tubulin. (D) Immunoblot analysis of NMHCII-A expression in A^{gfp}/A^+ lungs also shows similar expression of GFP–NMHCII-A compared with NMHCII-A. (E) Evidence for heterodimer formation in $A^{gfpR702C}/A^+$ mouse tissue. High-salt lysates of $A^{gfpR702C}/A^+$ lung tissue were incubated with anti-GFP, and the immunoprecipitate was subject to SDS-PAGE followed by immunoblotting with NMHCII-A Ab. Lane 1 indicates A^+/A^+ lysate immunoprecipitated with anti-GFP shows no immunoprecipitate; lane 2, $A^{gfpR702C}/A^+$ lysate treated with beads without Ab shows no immunoprecipitate; lane 3, $A^{gfpR702C}/A^+$ lysate immunoprecipitated with anti-GFP shows a 4-fold increase in GFP–NMHCII-A R702C compared with NMHCII-A; and lane 4, $A^{gfpR702C}/A^+$ lysate input showing endogenous NMHCII-A (bottom band) and GFP–NMHCII-A R702C (top band). The signal intensity ratio between the top band and bottom band of lane 3 is 4.09 ± 0.69 (n = 3), ratio for lane 4 is 0.81 ± 0.13 (n = 3). Relative intensity of signal was determined with ImageJ (NIH). (F,G) Immunoprecipitation from A^{gfp}/A^+ lung (F, lane 2) and leukocytes (G, lane 2) shows 5.25 ± 0.35 (n = 2) and 3.94 (n = 1) ratio of GFP–NMHCII-A to NMHCII-A, respectively. Lane 1 is immunoprecipitation with beads but without Ab, lane 2 is the immunoprecipitate with anti-GFP, and lane 3 is input.

constructs were targeted into the endogenous *Myh9* locus by standard homologous recombination methods.

As controls, mice were generated with GFP inserted into exon 2, in frame with the endogenous *Myh9* coding region, which results in GFP fused to the N-terminus of endogenously expressed NMHCII-A (supplemental Figure 1D). The GFP-tagged endogenous protein facilitates live-cell imaging by confocal and multiphoton microscopy. We refer to the wild-type allele as A^+, the mutant alleles as $A^{gfpR702C}$, A^{D1424N}, and A^{E1841K}, and the GFP-tagged A^+ allele as A^{gfp}. In all cases, the Neo^r cassette used for selection of embryonic stem cells has been removed by crosses to CMV-cre mice.

On the basis of immunoblot analysis, the protein expression level of GFP-NMHCII-A in the $A^{gfpR702C}/A^+$ mouse lung (Figure 1A), leukocytes/platelets fraction, MKs, and neutrophils (supplemental Figure 2A-B) is ~ 80% of the endogenous NMHCII-A level. NMII-B and NMII-C expression remains undetectable in the $A^{gfpR702C}/A^+$ platelets and leukocytes (supplemental Figure 2C-D). The expression levels of D1424N and E1841K mutant NMHCII-A are comparable to wild-type NMHCII-A (Figure 1B-C). As shown in Figure 1D, the expression level of the GFP-tagged NMHCII-A in the A^{gfp}/A^+ mouse tissue is the same as that of the endogenous NMHCII-A.

The presence of GFP in the GFP–NMII-A mice made it possible to determine whether a NMII-A molecule is composed of dimers of one mutant and one wild-type NMHC. To test whether heterodimeric NMII-A can form, protein extracts were obtained from A^{gfp}/A^+ and $A^{gfpR702C}/A^+$ mouse lung tissue, Abs against GFP were used to immunoprecipitate GFP–NMII-A, and subsequent SDS-PAGE was used to separate wild-type NMHCII-A and GFP-NMHCII-A. Immunoblotting with anti–NMHCII-A Ab shows that most, but not all, GFP–NMII-A R702C (Figure 1E lane 3) and GFP–NMII-A (Figure 1F lane 2) pulled down by the anti-GFP Ab is GFP-labeled. GFP–NMHCII-A R702C or GFP–NMHCII-A represent 4-5 times the amount of the wild-type NMHCII-A, indicating that as much as 20%-25% of the NMII could be heterodimers. A similar result is found for purified leukocytes/platelets (Figure 1G).

Embryonic lethality of $A^{gfpR702C}/A^{gfpR702C}$ but not A^{D1424N}/A^{D1424N} or A^{E1841K}/A^{E1841K} mice

In contrast to the matings of A^{D1424N}/A^+ and A^{E1841K}/A^+ mice, which resulted in the expected numbers of pups in normal Mendelian ratios, mating of $A^{gfpR702C}/A^+$ mice did not produce $A^{gfpR702C}/A^{gfpR702C}$ offspring (supplemental Table 2). The $A^{gfpR702C}/A^{gfpR702C}$ embryos die at approximately embryonic day (E) 11.5. At E10.5, $A^{gfpR702C}/A^{gfpR702C}$embryos are smaller than wild-type littermates and are developmentally delayed (supplemental Figure 3A). A histologic examination of the placenta

from A^+/A^+ and $A^{gfpR702C}/A^{gfpR702C}$ embryos at E10.5 shows the A^+/A^+ placentas acquire the normal trilaminar architecture (supplemental Figure 3B). The A^+/A^+ labyrinth layer has a porous appearance with well-organized trophoblast cells distributed around the fetal and maternal blood vessels. In contrast, the $A^{gfpR702C}/A^{gfpR702C}$ labyrinth layer is more compact with fewer maternal and fetal blood vessel spaces. These results suggest that the embryonic lethality of $A^{gfpR702C}/A^{gfpR702C}$ embryos results from the failure of fetal placental vascularization.

All mutant mouse lines show platelet abnormalities found in *MYH9*-RD

Macrothrombocytopenia is found in all mutant mouse lines. Images from blood smears (Figure 2Ai) show that normal platelets from the A^+/A^+ mouse are significantly smaller than erythrocytes. In contrast, the size of platelets in $A^{gfpR702C}/A^+$, A^{D1424N}/A^+, A^{E1841K}/A^+, A^{D1424N}/A^{D1424N}, and A^{E1841K}/A^{E1841K} mutant mice is more variable with some of the platelets as large or even larger than erythrocytes (Figure 2Aii-vi). Figure 2B shows a comparison of the MPV of the circulating platelets from heterozygous and homozygous mutants and A^+/A^+ mice. The MPVs from heterozygous and homozygous mutant mice are $\sim$ 1.5 and 3.5 times larger, respectively, than A^+/A^+ MPVs. To confirm the MPV results, the platelet diameters were directly measured from the blood smears, and they varied from 0.8 to 9.6 μm. As shown in Figure 2C, the platelet diameters from the mutant mice are significantly larger than platelet diameters from A^+/A^+ mice ($P < .001$). All of the mutant mice also have significantly lower platelet counts than wild-type mice (Figure 2D), although automated counts will not include large size platelets. Platelet function was also impaired as manifested by prolonged bleeding times (Figure 2E) and a partial failure in clot retraction (Figure 2F).

MKs are more numerous in the BM and spleen of mutant mice

To determine whether there are any defects in MKs that could account for the low platelet numbers and abnormal size of the mature circulating blood platelets, MKs in histologic sections of fixed femur BM and spleen were examined. The morphology of MKs in the BM of mutant NMII-A mice is similar to A^+/A^+ MKs. However, the mutant MKs are more numerous compared with the BM of A^+/A^+ littermates (Figure 3A arrows). The number of MKs in the BM of mutant mice is $\sim$ 100 MK/mm^2, which is significantly higher than that of A^+/A^+ littermates ($<$ 60 MKs/mm^2) (Figure 3B). In addition, sections of the spleen stained with a MK marker indicate an increase in MK number in the mutant mice (Figure 3C), which suggests an attempt to compensate for the decrease in platelet production from the mutant BM.

Careful examination of the femur BM showed numerous examples of neutrophil inclusions (emperipolesis) in the MKs of the A^{D1424N}/A^{D1424N} and A^{E1841K}/A^{E1841K} mice (Figure 3Di-ii arrows), which is rarely found in A^+/A^+ samples. These neutrophil inclusions were confirmed by EM (Figure 3Diii).

MK defects in $A^{gfpR702C}/A^+$ mice in culture detected by live-cell imaging

The presence of GFP-NMHCII-A R702C and control GFP-NMHCII-A permitted visualization in mouse tissues by confocal or multiphoton microscopy. MKs were cultured from the livers of E13.5 embryos and after thrombopoietin (TPO) stimulation for 3 days,[18] MKs at different stages of development and proplatelet formation (PPF) were observed. Because no structural differences between the A^+/A^+ and A^{gfp}/A^+ MKs in culture were observed (Figure 4Ai-ii), A^{gfp}/A^+ MKs were used as a control for fluorescence live-cell imaging. NMII-A is highly expressed in MKs at different developmental stages, and there is no apparent difference in initial cell structure or NMII-A distribution between MKs from A^{gfp}/A^+ mice and $A^{gfpR702C}/A^+$ mice. However, there are differences in PPF between MKs found in the A^{gfp}/A^+ and $A^{gfpR702C}/A^+$ mice. During the final stage of maturation, PPF can be observed in A^+/A^+, A^{gfp}/A^+, and $A^{gfpR702C}/A^+$ cultures (Figure 4A). NMII-A visualized by GFP can be seen not only within the cell body but also in the developing proplatelets (Figure 4A-B). In A^+/A^+ and A^{gfp}/A^+ mice each MK gives rise to numerous proplatelets that have multiple branches with multiple buds from which the platelets arise. In contrast, $A^{gfpR702C}/A^+$ MKs have substantially fewer proplatelets emanating from each MK. These proplatelets are usually shorter and have fewer branches (Figure 4Aiv and Biii-iv). Some proplatelets from the $A^{gfpR702C}/A^+$ MKs have thicker stalks than A^{gfp}/A^+ MKs, and there are fewer buds (Figure 4Biii-iv). (A^{D1424N}/A^{D1424N} MKs show a similar phenotype by differential interference contrast [DIC] imaging; data not shown.) To quantify the ability of MKs to produce proplatelets, the cultured cells were fixed and labeled with the MK marker CD41, and the percentage of the MKs with proplatelets was counted (Figure 4B-C). By day 4 in culture, $\sim$ 30.8% ± 12.6% of the MKs from A^+/A^+ littermates have formed proplatelets compared with 7.4% ± 1.9% of the $A^{gfpR702C}/A^+$ MKs (*t* test, $P < .001$; Figure 4C). The size of proplatelet buds from both A^{gfp}/A^+ and $A^{gfpR702C}/A^+$ MK cultures was also quantified from confocal images because the GFP signal is easily detected and the measurement is more accurate. The size of the $A^{gfpR702C}/A^+$ proplatelet buds (5.84 ± 2.73 μm) is significantly increased compared with A^{gfp}/A^+ (3.07 ± 1.05 μm; Mann-Whitney rank sum test, $P < .001$; Figure 4D), which is reminiscent of the enlarged size of the peripheral blood platelets.

In an effort to study platelet release in vitro MKs were isolated and subjected to conditions mimicking flow.[19] Results in Figure 4E-F show that $A^{gfpR702C}/A^+$ proplatelets release larger platelets of various diameter compared with the consistently small platelets of A^+/A^+ embryonic littermates.

Live sternal BM imaging of MK PPF

To confirm the results from the culture system, MKs in the BM were examined in situ by confocal and multiphoton microscopy. The presence of GFP in both the mutant and control mice made it possible to monitor PPF in the MK's native BM niche. Imaging on freshly euthanized A^{gfp}/A^+ mice or $A^{gfpR702C}/A^+$ mice was performed by removal and bisection of the sternum in the sagittal plane as previously described.[16] Imaging was also performed in femur, calvaria and spleen; supplemental Figure 4. Like in vitro cultures of MKs, the morphology of MKs before PPF in the mutant $A^{gfpR702C}/A^+$ BM is similar to control A^{gfp}/A^+ MKs, but numbers are markedly increased in the mutant (80/mm^3) compared with control (50/mm^3) sternum BM.

Examination of the dynamic process of PPF in situ in the BM shows the differences between control and mutant MKs. MKs are mostly immobile compared with highly dynamic neutrophils that can be observed moving throughout the tissue. Highly motile neutrophils are often seen scanning and pulling at the surface of MKs (supplemental Video 1). Although MKs are not synchronized and only a limited number undergo maturation and PPF, we imaged thrombopoiesis involving mostly MKs in proximity to bone structures. Occasionally, cells were followed over 3-4 hours until

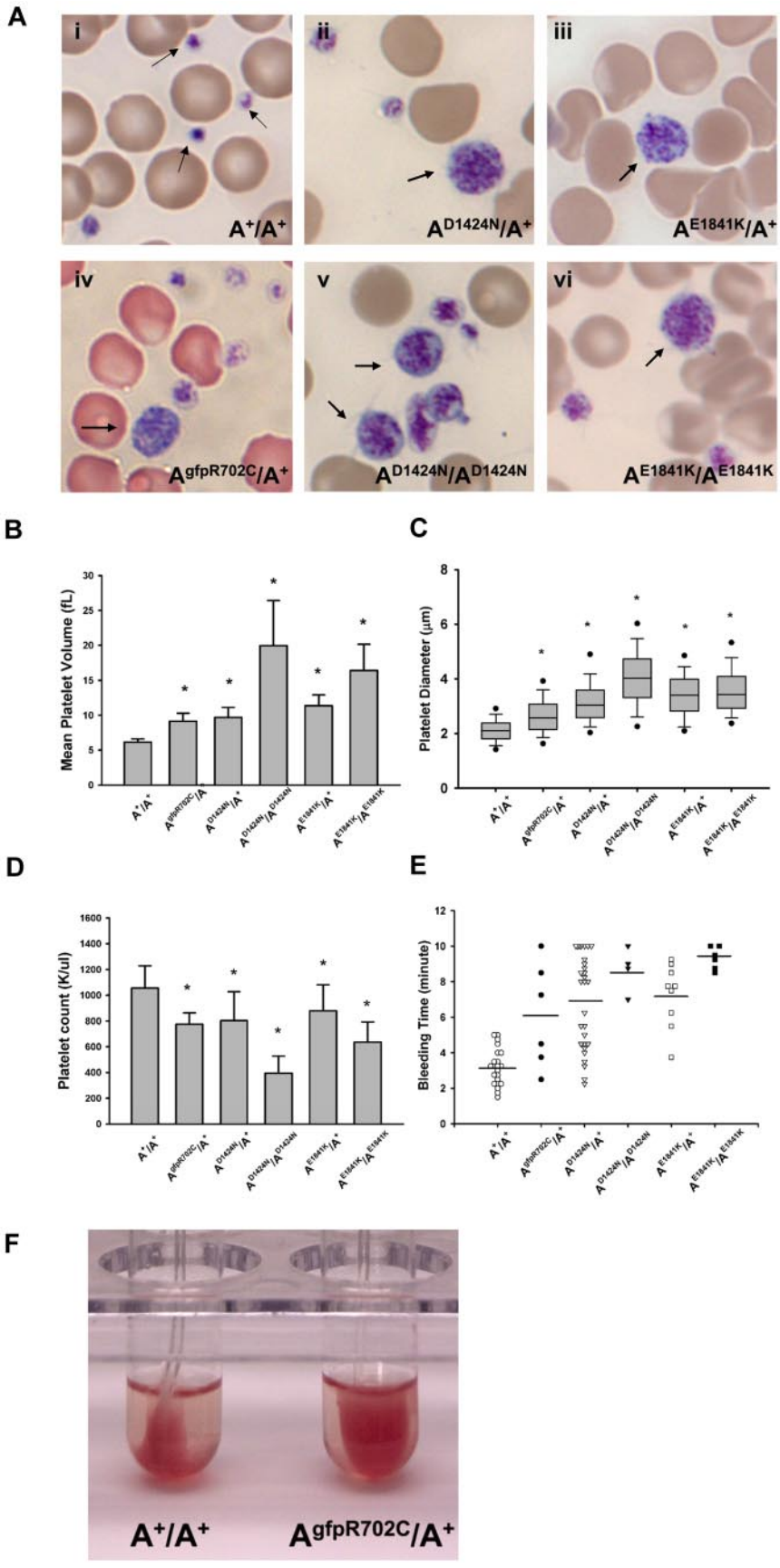

Figure 2. Platelet analyses in NMII-A mutant and control mouse blood. (Ai) Blood smear from an A^+/A^+ mouse shows normal size platelets (arrows), approximately one-tenth the diameter of erythrocytes. (Aii-vi) Giant platelets (arrows) with a size close to that of erythrocytes were easily detected in blood smears from all 3 mutant mouse lines. Blood smears are stained with Wright-Giemsa stain. (B) Mean platelet volumes (MPVs) of circulating platelets. MPVs from heterozygous and homozygous mutant mice are all significantly larger than the MPV from A^+/A^+ mice. Results represent mean ± SD. A^+/A^+ MPVs: 6.15 ± 0.45 fL (n = 18); $A^{gfpR702C}/A^+$: 9.13 ± 1.16 fL (n = 12); A^{D1424N}/A^+: 9.67 ± 1.44 fL (n = 10); A^{D1424N}/A^{D1424N}: 19.95 ± 6.45 fL (n = 4); A^{E1841K}/A^+: 11.37 ± 1.53 fL (n = 13); and A^{E1841K}/A^{E1841K}: 16.40 ± 3.75 fL (n = 3). *$P < .001$, 1-way ANOVA compared with A^+/A^+. (C) Platelet diameters measured from peripheral blood smears. Platelet diameters (mean ± SD) of A^+/A^+: 2.12 ± 0.45 μm (n = 193); $A^{gfpR702C}/A^+$: 2.67 ± 0.78 μm (n = 225); A^{D1424N}/A^+: 3.19 ± 0.93 μm (n = 110); A^{D1424N}/A^{D1424N}: 4.01 ± 1.09 μm (n = 114); A^{E1841K}/A^+: 3.41 ± 0.88 μm (n = 169); and A^{E1841K}/A^{E1841K}: 3.63 ± 1.01 μm (n = 158). The box plot shows median, upper and lower quartiles, and upper and lower 5 percentiles of each group. *$P < .001$ 1-way ANOVA compared with A^+/A^+. Platelet diameter was measured on images of Wright-Giemsa–stained blood smears with the use of ImageJ (NIH). (D) Platelet counts from peripheral blood. Platelet counts from heterozygous NMII-A mutant mice are all significantly lower than those of A^+/A^+ mice, and homozygous mutant mice have even lower platelet counts. Results represent mean ± SD. Circulating platelet counts of A^+/A^+: 1056.29 ± 172.23 K/μL (n = 21); $A^{gfpR702C}/A^+$: 774.67 ± 88.02 K/μL (n = 12); A^{D1424N}/A^+: 801.90 ± 225.76 K/μL (n = 22); A^{D1424N}/A^{D1424N}: 395.40 ± 131.80 K/μL (n = 5); A^{E1841K}/A^+: 878.79 ± 202.31 K/μL (n = 14); and A^{E1841K}/A^{E1841K}: 635.33 ± 157.15 K/μL (n = 3). *$P < .001$, 1-way ANOVA compared with A^+/A^+. (E) Tail bleeding times. Mutant mice have a prolonged tail bleeding time compared with A^+/A^+ mice. Bar indicates mean of each group. (F) Clot retraction test. Representative image shows that the $A^{gfpR702C}/A^+$ platelet sample (in right tube) has reduced clot retraction compared with the A^+/A^+ sample (left tube). Image was taken 3 hours after stimulation.

thrombopoiesis was almost complete (supplemental Video 2). Figure 5A shows examples of PPF in A^{gfp}/A^+ mouse samples (supplemental Video 3). Figure 5C shows images of 1 of 2 MKs undergoing PPF in control A^{gfp}/A^+ mouse samples (supplemental

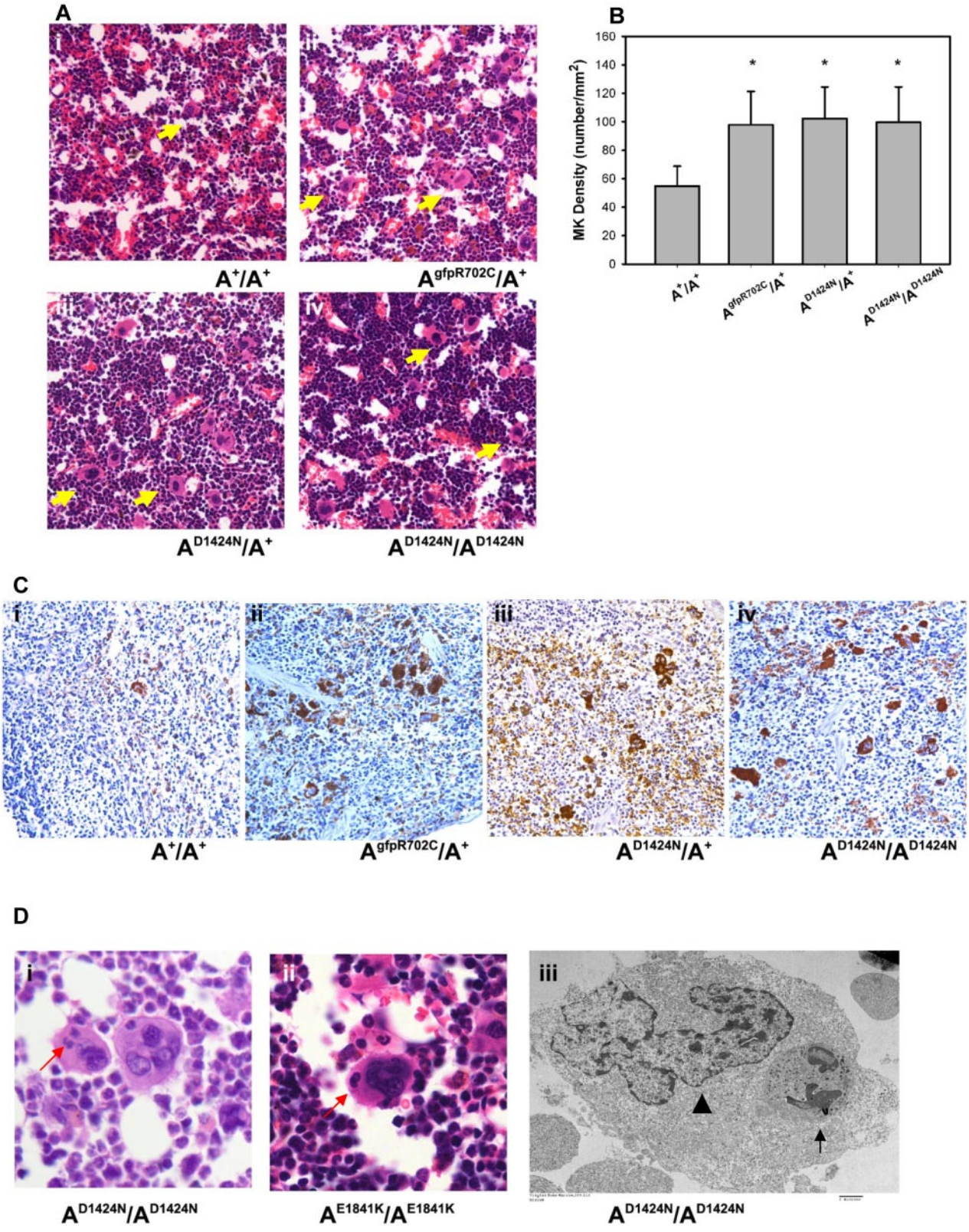

Figure 3. Abnormalities in mutant MKs. (A) Representative images of MKs (yellow arrows) in H&E-stained sections of mouse femur BM from (Ai) A^{+}/A^{+} and (Aii-iv) mutant mice. (B) MK densities quantified from H&E-stained femur BM sections. Results represent mean ± SD. A^{+}/A^{+}: 54.84 ± 14.02 (n = 6); $A^{gfpR702C}/A^{+}$: 99.24 ± 16.26 (n = 7); A^{D1424N}/A^{+}: 102.38 ± 22.16 (n = 4); A^{D1424N}/A^{D1424N}: and 99.68 ± 24.89 (n = 4). *P = .001 1-way ANOVA compared with A^{+}/A^{+}. (C) MKs in spleens from A^{+}/A^{+} (Ci) and mutant (Cii-iv) mice at 4-6 months of age. Note the increased number of MKs in spleens from the mutant mice. Brown stain indicates VWF; and blue stain, hematoxylin. (D) MK emperipolesis (neutrophil inclusions in MK cells) in A^{D1424N}/A^{D1424N} and A^{E1841K}/A^{E1841K} mouse femur BM. (Di-ii) One or 2 neutrophils (red arrows) are seen in the MKs in H&E-stained sections. (Diii) EM image of an A^{D1424N}/A^{D1424N} MK shows a neutrophil (arrow) inside the cytoplasm of a MK. The MK nucleus is indicated by an arrowhead.

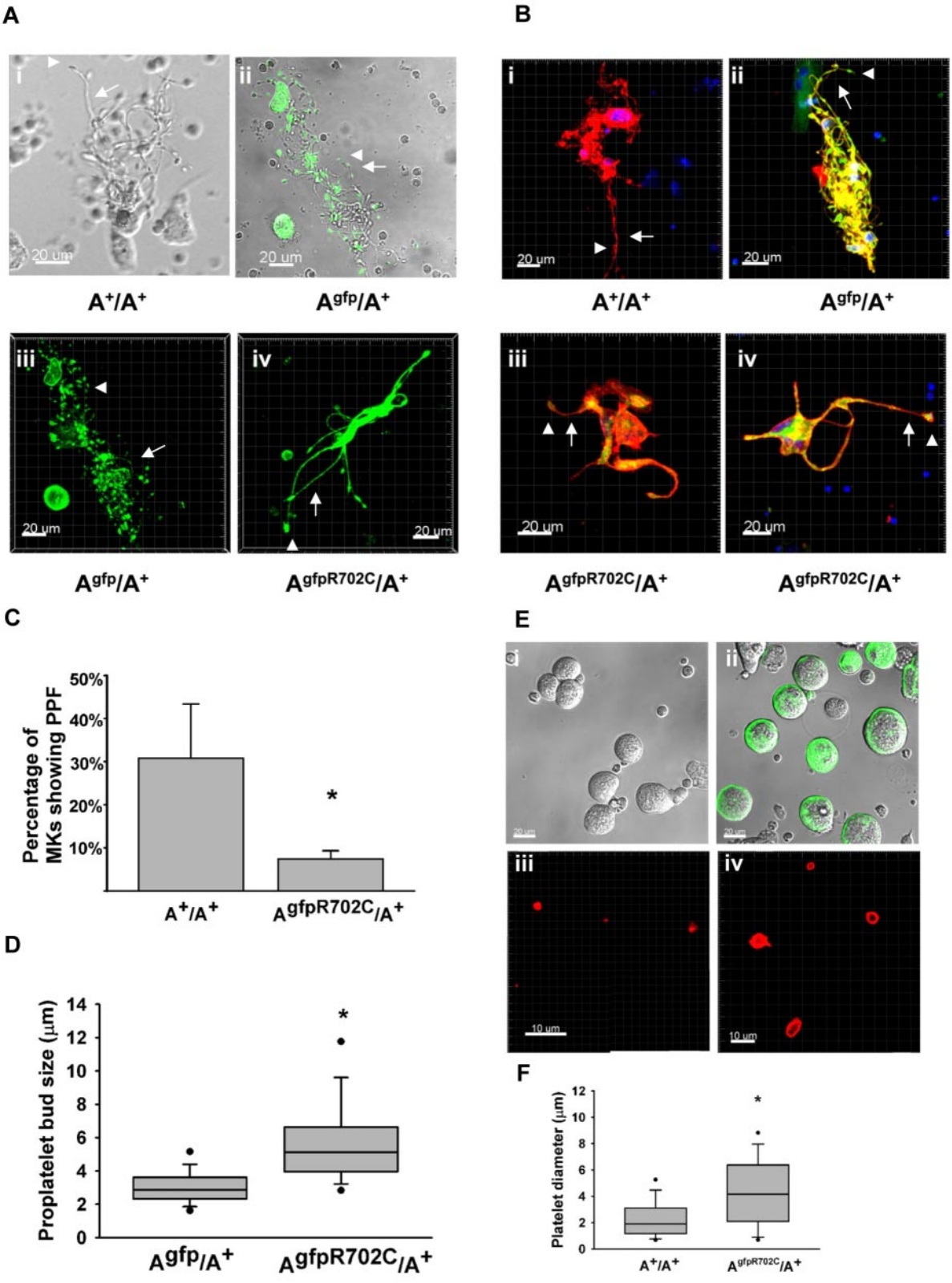

Figure 4. MK culture and PPF from fetal liver. (A) Live-cell images of MKs cultured from fetal liver of A^{+}/A^{+}, A^{gfp}/A^{+}, and $A^{gfpR702C}/A^{+}$ embryos. Phase image is shown for A^{+}/A^{+} (Ai), fluorescence/DIC overlay image for A^{gfp}/A^{+} (Aii), and fluorescence z-stack images for A^{gfp}/A^{+} (Aiii) and $A^{gfpR702C}/A^{+}$ (Aiv). Arrows indicate proplatelets; arrowheads, platelet buds; green: GFP. Bar, 20μm. (B) Fixed MK cultures stained with anti-CD41 to confirm the identity of the MKs. Note the difference in the length and thickness of the proplatelets (arrows) and the size of the proplatelet buds (arrowheads) between control (Bi-ii) and $A^{gfpR702C}/A^{+}$ (Biii-iv) MKs. Red indicates CD41; and green, GFP. Bar, 20 μm. (C) Percentage of MKs undergoing PPF in culture (mean ± SD). A^{+}/A^{+}: 30.8% ± 12.6% (n = 5); and $A^{gfpR702C}/A^{+}$: 7.4% ± 1.9% (n = 9). $^{*}P < .001$ (*t* test). (D) Proplatelet bud size in culture. Measurements of the diameters of proplatelet buds are from the confocal microscope images of live A^{gfp}/A^{+} and $A^{gfpR702C}/A^{+}$ MKs. Box plot shows median, upper and lower quartiles, and upper and lower 5 percentiles of each group. A^{gfp}/A^{+}: 3.07 ± 1.05 μm (n = 199); and $A^{gfpR702C}/A^{+}$: 5.84 ± 2.73 μm (n = 107); $^{*}P < .001$ (*t* test). (E) In vitro production of platelets from A^{+}/A^{+} and $A^{gfpR702C}/A^{+}$ embryonic littermate MKs. DIC imaging shows A^{+}/A^{+} (Ei) and $A^{gfpR702C}/A^{+}$ (Eii; GFP signal included) MKs separated from 4-day fetal liver culture by 1.5%-3.0% BSA gradient before PPF; (Eiii-iv) immunofluorescence staining with CD41 Ab to identify platelets after in vitro platelet production by shaking at 150 rpm for 2 hours at 37°. (F) Quantitation of platelet diameter from A^{+}/A^{+} and $A^{gfpR702C}/A^{+}$ in vitro platelet production.

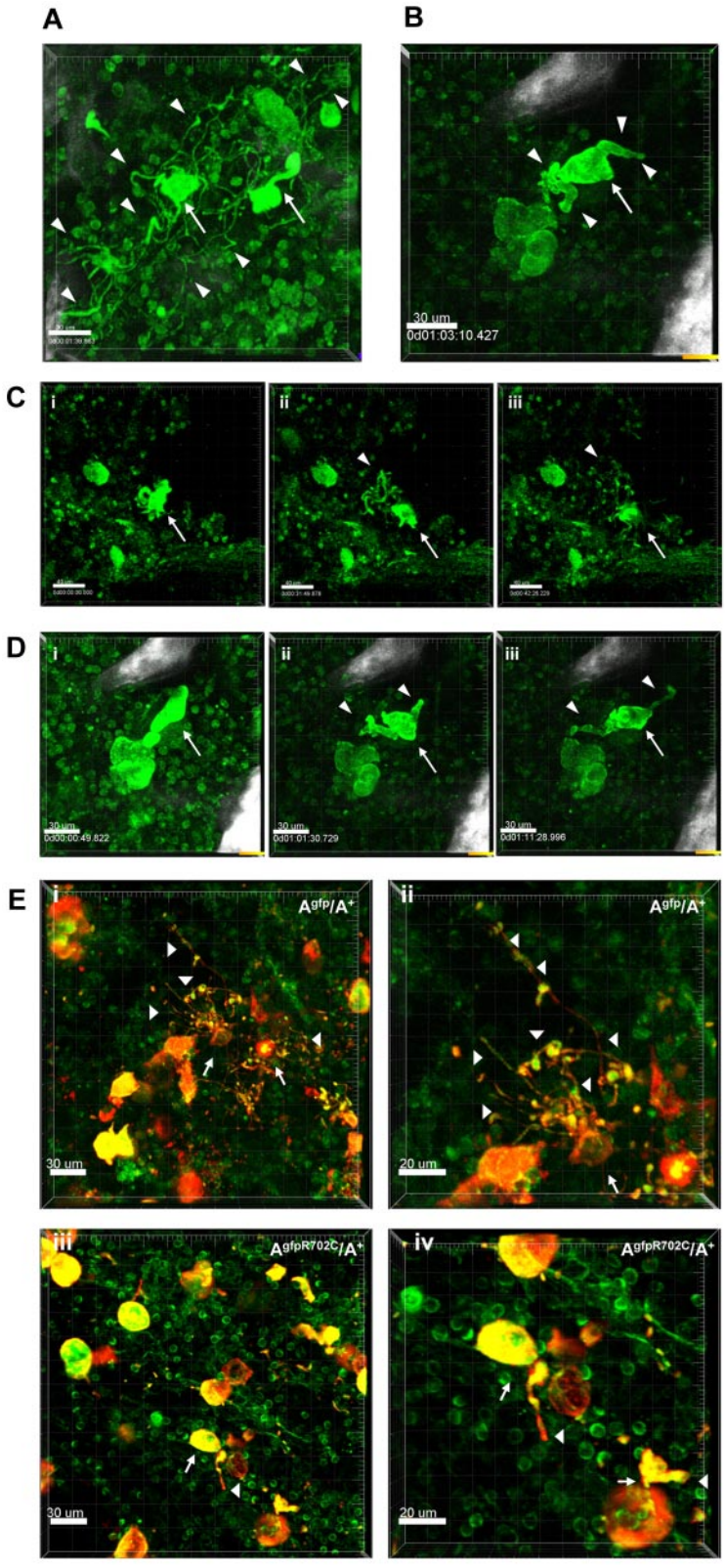

Figure 5. Live tissue imaging of BM from A^{gfp}/A^{+} and $A^{gfpR702C}/A^{+}$ mice. (A) Representative 3D images of MKs in control A^{gfp}/A^{+} BM (n = 9). There are 2 MKs (arrows) forming proplatelets (arrowheads indicate some of the proplatelets). The well-developed multiple branches of proplatelets and the multiple buds are similar to those seen in culture. Bar, 30 μm. (B) Representative 3D image from a video showing a MK (arrow) during PPF in $A^{gfpR702C}/A^{+}$ BM (n = 7). The mouse shown was injected with 1 ng TPO/g of body weight 3 days before imaging to increase possibility of visualizing PPF.[21] Proplatelets are shorter and thicker than those seen in panel A. White signal is due to bone collagen SHG. Bar, 30 μm. (C) Snapshot from supplemental Video 2 of a MK (arrow) in A^{gfp}/A^{+} BM. Proplatelets and buds are indicated by arrowheads. Bar, 40 μm. (D) Snapshots from a video showing PPF from a MK (arrow) in $A^{gfpR702C}/A^{+}$ BM. There are fewer branches and buds on proplatelets (arrowheads; supplemental Video 5). White signal is because of bone collagen SHG. Bar, 30 μm. (E) Fixed BM confirming MK identity by CD41 staining in A^{gfp}/A^{+} (Ei-ii) and $A^{gfpR702C}/A^{+}$ (Eiii-iv) BM. (Eii,iv) Shown are increased magnification of panel Ei,iii. Arrows indicate MKs; arrowheads, proplatelets; red, CD41; green, GFP. Bar, 30 μm (Ei,iii) and 20 μm (Eii,iv).

Video 2). Similar to the experiments in culture, in situ proplatelets from control MKs appear thin and well-branched. The process of PPF is dynamic, with nascent proplatelets attached to the MK cell body being pulled back and forth (supplemental Video 3). Very long processes (150 μm) often extend in proximity to the bone which acts as a support, and numerous proplatelet buds (10-15) appear aligned and moving at once as "beads on a string"(supplemental Video 4). However, platelet release from MKs is not observed, suggesting the important role played by blood flow, which is absent in BM in situ experiments.[20] PPF in $A^{gfpR702C}/A^{+}$ samples is much less frequent than in control A^{gfp}/A^{+} samples, although MKs are more numerous than in control samples. (To

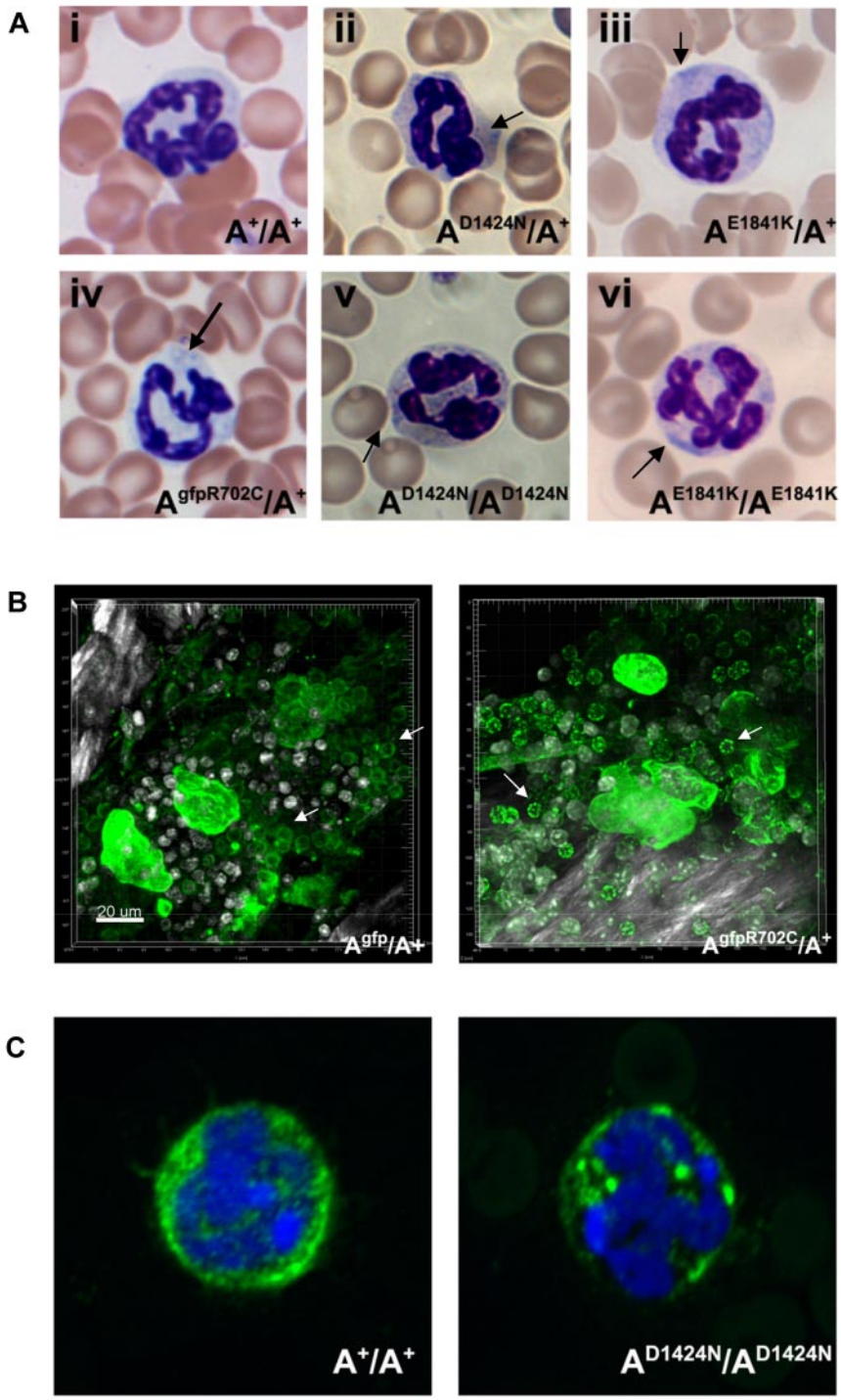

Figure 6. Neutrophil inclusion bodies in NMII-A mutant mice. (A) Representative images show inclusion bodies (arrows) that were found in neutrophils from mutant (Aii-vi) but not control (Ai) mouse blood smears. Blood smears are stained with Wright-Giemsa. (B) Live cell imaging of neutrophils (arrows) from A^{gfp}/A^{+} and $A^{gfpR702C}/A^{+}$ mouse BM. The NMII-A in $A^{gfpR702C}/A^{+}$ neutrophils is more heterogeneous and punctate compared with NMII-A in the A^{gfp}/A^{+} control. Green indicates GFP signal; white signal, bone collagen SHG; and white spots, Hoechst-stained nuclei. Bar, 20 μm. (C) Immunofluorescence confocal images of fixed neutrophils from A^{+}/A^{+} and A^{D1424N}/A^{D1424N} mice. NMHCII-A (green) is distributed in the cytoplasm of the A^{+}/A^{+} neutrophil. Mutant NMHCII-A D1424N aggregates into circular to oval-shaped cytoplasmic spots in A^{D1424N}/A^{D1424N} neutrophil. DAPI (blue) stains nuclei.

increase PPF, an $A^{gfpR702C}/A^{+}$ mouse was injected with 1 ng TPO/g of body weight.[21]) In the cases in which PPF in $A^{gfpR702C}/A^{+}$ BM was observed (Figure 5B; supplemental Video 5), the proplatelets are short and less branched, and the stalks of proplatelets are much thicker than those seen in control MKs. Figure 5D shows images of the PPF process from an $A^{gfpR702C}/A^{+}$ sample (supplemental Video 5). Figure 5E compares fixed BM from A^{gfp}/A^{+} and $A^{gfpR702C}/A^{+}$ samples stained with anti-CD41 Ab to confirm the identity of MKs and platelets. Thus, PPF is impaired in mutant $A^{gfpR702C}/A^{+}$ BM compared with control. Although the mutant $A^{gfpR702C}/A^{+}$ mice have more MKs in the BM, the probability of the MK undergoing PPF is low, and fewer proplatelets extend from each mutant MK, with fewer branches and thicker stalks and buds.

Evidence for NMII-A aggregation in neutrophils

Neutrophil inclusions in blood from patients are thought to contain aggregates of mutant NMII-A.[22] Figure 6A (arrows) shows the presence of these aggregates in the neutrophils of all the mutant mice. With the use of live-tissue imaging of BM, a marked increase was noted in aggregates of NMII-A in $A^{gfpR702C}/A^{+}$ compared with A^{gfp}/A^{+} neutrophils (Figure 6B). Similar findings were also noted

in fixed A^{D1424N}/A^{D1424N} neutrophils with the use of immunofluorescence confocal microscopy (Figure 6C).

Cataracts in D1424N and E1841K mutant mice

Cataracts, in most cases bilateral, are found in some of the A^{D1424N}/A^{+} and A^{D1424N}/A^{D1424N} and A^{E1841K}/A^{+} mice but not to date in R702C mice. Supplemental Figure 5Bi shows an example of a cataract found in a 6-month-old A^{E1841K}/A^{+} mouse and a normal lens from an A^{+}/A^{+} mouse (supplemental Figure 5Ai). The lens in the A^{E1841K}/A^{+} eye showed diffuse cataract changes, including swelling, lens epithelial proliferation and degeneration, and liquefaction of lens fibers (supplemental Figure 5Bii-iv). In contrast to the normal cornea of the A^{+}/A^{+} mouse, corneal neovascularization (arrow) and mild inflammatory cellular infiltration is seen in the A^{E1841K}/A^{+} mouse cornea (supplemental Figure 5C).

Hearing thresholds

Thresholds of auditory-evoked brainstem responses were determined in heterozygous mutant mice (8-14 months old). Normal auditory-evoked brainstem response thresholds and waveforms were observed in control littermates for each mutant strain. The A^{R702C}/A^{+}, A^{D1424N}/A^{+}, and A^{E1841K}/A^{+} mice stimulated at 8-,16-, and 32-kHz tone bursts or 31-μsec duration clicks show increased hearing thresholds for the A^{E1841K}/A^{+} mice compared with littermate controls (supplemental Table 3). The A^{E1841K}/A^{+} mice also show a progressive hearing loss with age (supplemental Table 4).

Kidney abnormalities in the point mutant and NMII-A podocyte-ablated mice

Patients with *MYH9*-RDs manifest glomerulopathy, characterized by albuminuria and progressive glomerulosclerosis, in some cases manifesting as focal segmental glomerulosclerosis (FSGS) and sometimes accompanied with glomerular basement membrane abnormalities.[23] In the mice, the earliest pathologic changes, beginning at ~ 4 months of age, were FSGS and focal global glomerulosclerosis (Figure 7Aii-iv). All kidney sections also showed normal glomeruli, indicating that glomerulopathy begins as a focal process and is thus consistent with FSGS. Supplemental Figure 6 shows the range of appearance of glomeruli from a single A^{E1841K}/A^{+} kidney. In general the pathologic lesions observed were less frequent and less severe in the $A^{gfpR702C}/A^{+}$ mice. Figure 7B shows the range of urine albumin/creatinine ratios for the mutant mouse lines (see also supplemental Figure 6B). Previous work from human patients has suggested that the abnormalities found in the kidneys could reflect defects in the podocytes.[24] NMII-A partially colocalizes with the podocyte marker, synaptopodin in both A^{gfp}/A^{+} and $A^{gfpR702C}/A^{+}$ glomeruli (Figure 7C). Figure 7D provides evidence for altered podocyte architecture, typically foot process effacement, that is seen in the A^{D1424N}/A^{D1424N} mice. Similar defects were seen in each of the mutant mice, suggesting the idea that the defect in the podocytes was at least partially responsible for the kidney abnormality.

Mice that were ablated for NMII-A exclusively in podocytes were generated to investigate whether specific deletion in podocytes would result in a phenotype similar to that of the mutant mice. Mice in which exon 3 of *Myh9* and the Neo^{r} cassette are floxed[14] were crossed with mice in which cre recombinase is expressed under control of the podocin promoter.[15] Supplemental Figure 7A shows sections of glomeruli from A^{+}/A^{+} mice and conditionally ablated NMII-A mice A^{pod}/A^{pod} with glomerulosclerosis present in the latter. A Coomassie blue-stained SDS-polyacrylamide gel showing an example of the albuminuria in the A^{pod}/A^{pod} mice is shown (supplemental Figure 7B). Figure 7E contrasts the normal morphology of an A^{+}/A^{+} cre^{+} mouse (supplemental Figure 7Bi,iii) with that of an A^{pod}/A^{pod} mouse (supplemental Figure 7Bii,iv) with the use of scanning EM (supplemental Figure 7Bi,ii) and transmission EM (supplemental Figure 7Biii,iv). Note the distortion of and altered structure of podocyte processes found in the A^{pod}/A^{pod} glomeruli by scanning EM and podocyte effacement with loss of the filtration slits (quantification provided in the figure legend).

Summary of the phenotypes observed

All 5 mutant mouse lines show platelet abnormalities, including an increased MPV, increased diameter, and a decreased platelet count. The 2 homozygous lines (D1424N and E1841K) show the greatest changes. A decrease in proplatelet formation and an increase in platelet bud size were observed by immunofluorescence in the $A^{gfpR702C}/A^{+}$ mice and by DIC imaging for A^{D1424N}/A^{+} and A^{D1424N}/A^{D1424N} mice. All of the mutant lines had Döhle bodies.

Cataracts were seen in some A^{D1424N}/A^{+}, A^{D1424N}/A^{D1424N}, and A^{E1841K}/A^{+} mice.

Hearing loss has only been found in the A^{E1841K}/A^{+} mice, although only heterozygotes have been tested to date.

All 5 mutant mouse lines show evidence for glomerulosclerosis with abnormal albumin/creatinine ratios.

Discussion

We have generated mouse models of the 3 most common human mutations that cause *MYH9*-RD, R702C, D1424N, and E1841K, 1 mutation in the globular head, and 2 in the rod domain. To facilitate live-tissue microscopy and to duplicate the human protein, GFP was fused to human cDNA with the R702C mutation and was used to replace the endogenous mouse NMHCII-A. The expression level of the GFP-NMHCII-A R702C was ~ 80% of the A^{+}. The other 2 mutations were introduced directly into the relevant mouse exon, and mutant expression levels were the same as the wild-type protein.

All 5 mutant mouse lines reproduce the human phenotype with respect to the hematologic defects in the platelets (macrothrombocytopenia) and also mimic the functional defects, including a prolonged bleeding time and decreased ability to retract clots. The defects in platelets appear to be caused by a failure in PPF in the MKs. This failure was studied by live-cell imaging in the BM of the $A^{gfpR702C}/A^{+}$ mice which shows a marked decrease in the initiation of PPF: decreased length of proplatelets and increased diameter of proplatelets and proplatelet buds. These findings were confirmed for $A^{gfpR702C}/A^{+}$ mice (and A^{D1424N}/A^{+} and A^{D1424N}/A^{D1424N} mice; data not shown) with the use of cultured MKs. The failure in PPF is in contrast to studies on MKs derived from NMII-A–ablated embryonic stem cells or on MKs derived from conditionally ablated mice in which NMII-A loss may initiate premature PPF and release of platelets.[25-28] In these cases loss of NMII-A appears to promote, rather than inhibit, PPF as shown for NMII-A mutations in the current report. This may be accounted for by the difference between ablation of NMII-A and expression of a poorly functioning mutant NMII-A.[29] Data from all mutant mouse lines show the same defects with respect to MK density in the BM, emperipolesis of the MKs, and Döhle body formation in the neutrophils.

The NMII-A point mutant and podocyte-specific NMII-A–deleted mice manifest podocyte abnormalities, albuminuria, FSGS, and progressive glomerulosclerosis. These changes closely

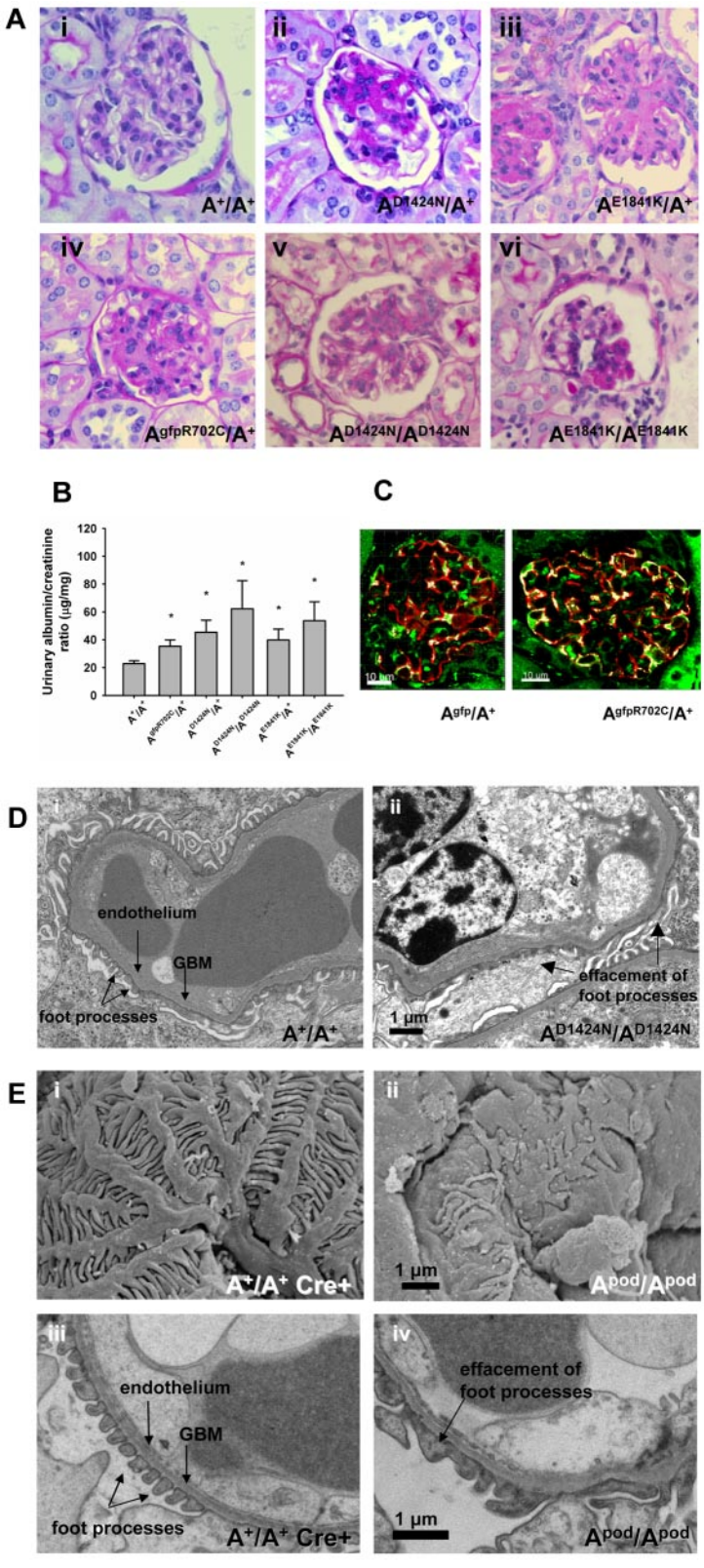

Figure 7. Kidney phenotype of NMII-A mutant mice. (A) Representative glomeruli from mutant mice show various stages of glomerulosclerosis in both heterozygous and homozygous glomeruli from segmental (Avi) to more nearly global (Aii-v). PAS-stained sections. Ages and sexes are (Ai) 9-month and female, (Aii) 6-month female, (Aiii) 12-month female, (Aiv) 12-month male, (Av) 9-month female, and (Avi) 7-month male. (B) Bar graph showing albumin/creatinine ratios in urine from mutant and A^{+}/A^{+} mice. All the mutant mouse lines show increased albumin excretion (13 of 44 for A^{R702C}/A^{+}, 11 of 28 for the A^{D1424N}/A^{+}, and 4 of 11 for the A^{E1841K}/A^{+}) compared with A^{+}/A^{+} mice. $^{*}P = .044$, 1-way ANOVA, mean ± SEM. (C) Immunofluorescence confocal images of A^{gfp}/A^{+} and $A^{gfpR702C}/A^{+}$ kidney glomeruli stained with anti-GFP (green) and anti-synaptopodin (red) showing localization of NMII-A in the podocytes. DAPI (blue) stains nuclei. Bar, 20 μm. (D) Transmission EM showing podocyte foot process effacement (arrow) in A^{D1424N}/A^{D1424N} glomerulus compared with A^{+}/A^{+} foot processes. Scanning (Ei-ii) and transmission (Eiii-iv) EM images of A^{+}/A^{+} cre^{+} and A^{pod}/A^{pod} glomeruli. The A^{pod}/A^{pod} podocytes are notable for shortened primary and secondary processes and reduced numbers of foot processes and filtration slits between the foot processes. Foot process widths (arbitrary units) were measured from the transmission EM obtained from 1 mouse of each genotype with the use of ImageJ (NIH): A^{+}/A^{+} cre^{+}: 0.105 ± 0.06, n = 371; and A^{pod}/A^{pod}: 0.319 ± 0.35, n = 293. GBM indicates glomerular basement membrane.

resemble those reported in human subjects with *MYH9*-RD. A recent report describes a podocyte-ablated NMII-A mouse that has normal kidney function and histology but shows an enhanced propensity to develop glomerulosclerosis in response to doxorubicin hydrochloride.[30] The difference with our finding of spontaneous kidney disease may be because of strain differences because our A^{pod}/A^{pod} are on a mixed background rather than back-crossed to C57BL/6 mice, which are resistant to glomerulosclerosis.[31] Although the pathogenesis of the glomerular disease is uncertain, podocyte expression of the mutant gene is probably the critical determinant, because genetic FSGS in humans has been associated with mutations in > 20 genes, all expressed in the podocyte.[32]

With respect to an underlying mechanism, we have ruled out both simple haploinsufficiency because of absence of NMII-A and a dominant-negative mechanism in which the mutant myosin interferes with the function of the wild-type NMII-A. Simple haploinsufficiency is ruled out because the expression level of the mutant NMHCII-A is the same as wild-type NMHCII-A in the D1424N and E1841K mice and is 80% of the wild-type in the GFP-R702C mouse. Moreover, live imaging of $A^{gfpR702C}/A^{+}$ BM clearly shows the expression of the mutant NMII-A in MKs and platelets. Previous work did not uncover evidence for hematologic, kidney, eye, or hearing defects in heterozygous A^{-}/A^{+} mice.[33,34] A straight-forward dominant-negative mechanism is ruled out because the homozygous D1424N and E1841K mice show the same defects as the heterozygous mice. Thus, the abnormalities seen in the mutant mice cannot simply be explained by mutant NMII-A interfering with wild-type NMII-A. It is possible that the mutant NMII-A is interfering with NMII-B or NMII-C but that cannot explain the defects seen in blood cells such as platelets and leukocytes in which NMII-A is the only isoform expressed.

The presence of the mutation in either the globular head or the rod region of the molecule is sufficient to impair the normal properties of myosin, which require the formation of bipolar filaments. These filaments are most probably composed of a mixture of heterodimers and homodimers of both the mutant and wild-type heavy chains. Abnormalities in these bipolar filaments, which are common to all 3 mutant NMII-As, could explain why defects in the different domains of NMII-A result in similar phenotypes. The commonality of bipolar filaments composed of mutant molecules could also explain why the homozygous mutants develop a more severe phenotype than the heterozygotes.

Our data support the utility of these mouse models of the human disease with respect to the phenotype found in the blood, eyes, and kidneys. They also resemble the human disease in that heterozygous mutations in the head and rod result in similar phenotypes. It should be pointed out that reports on humans allude to *MYH9*-RDs being more severe in patients with mutations in the motor than in the rod domain.[8,10] This was not observed with these mice, although genetic make-up and the relatively more inbred nature of the mice undoubtedly contribute to these differences. Our ability to study homozygous mice, which show similar but more severe abnormalities for the rod mutations, may help to define a mechanism and are also applicable to human homozygosity in *MYH9*-RD, which has been reported.[35] These mice afford the chance to investigate as yet unrecognized cellular defects because of NMII-A mutations. In addition, they can serve as important and useful in vivo models for studying the pathophysiology of the hematologic, renal, and ocular defects of *MYH9*-RD and for opening a path for new therapies.

Acknowledgments

The authors thank Drs Jack Levin (UCSF), Xuefei Ma, Sachiyo Kawamoto, and James R. Sellers, National Heart, Lung, and Blood Institute (NHLBI) for their incisive comments, useful discussions, and critical readings of the manuscript and Neal S. Young for encouragement with live GFP imaging. They thank Dalton Saunders for excellent technical assistance and acknowledge the expert assistance of the NHLBI Confocal Core Facility, Shervin Esfahani of the NHLBI Electron Microscopy Core Facility, the National Institutes of Health (NIH) Clinical Center Chemistry Laboratory, and the technicians in the NHLBI mouse facilities. Y.Z. especially thanks Katherine Calvo of the Clinical Hematology Laboratory for helpful discussions.

This work is supported by Division of Intramural Research, NHLBI, and the National Institute of Diabetes and Digestive and Kidney Diseases, (NIH grant R01HL66192, M.J.K.), and Deafness Research Foundation (M.J.K.). M.J.K. is the recipient of a Merit Review Award from the Department of Veterans Affairs.

This article is dedicated to the memory of Charles J. Epstein MD, outstanding scientist and physician and a pioneer in this field.

Authorship

Contribution: Y.Z. designed and performed experiments, generated the GFP-R702C and GFP-II-A mouse lines, characterized all mutant and control mouse lines, and wrote the manuscript; M.A.C. generated and characterized the conditional NMII-A null mice and wrote the manuscript; D.M. performed 2-photon and confocal live tissue imaging and helped write the manuscript; A.W. and Y.A.S. generated the D1424N mice; A.W. contributed to generation of the GFP-R702C mouse line; C.L. generated all transgenic mice except the E1841K; P.Z. performed the transmission EM; M.P.D. performed the scanning EM; C-C.C. reviewed the slides of the eyes and helped write the manuscript; E.K. performed hearing tests, analyzed the data, and helped write the manuscript; B.K. analyzed the hearing data and helped write the manuscript; M.J.K. designed experiments; F.D. generated the E1841K mutants; J.B.K. reviewed the slides of the kidneys, designed experiments, and helped write the manuscript; and R.S.A. directed research and wrote the manuscript.

Conflict-of-interest disclosure: The authors declare no competing financial interests.

Correspondence: Robert S. Adelstein, Laboratory of Molecular Cardiology, NHLBI, NIH, Bethesda, MD 20892-1583; e-mail: adelster@mail.nih.gov.

References

1. Heath KE, Campos-Barros A, Toren A, et al. Nonmuscle myosin heavy chain IIA mutations define a spectrum of autosomal dominant macrothrombocytopenias: May-Hegglin anomaly and Fechtner, Sebastian, Epstein, and Alport-like syndromes. *Am J Hum Genet.* 2001;69(5):1033-1045.
2. Kelley MJ, Jawien W, Ortel TL, Korczak JF. Mutation of MYH9, encoding non-muscle myosin heavy chain A, in May-Hegglin anomaly. *Nat Genet.* 2000;26(1):106-108.
3. Seri M, Cusano R, Gangarossa S, et al. Mutations in MYH9 result in the May-Hegglin anomaly, and Fechtner and Sebastian syndromes. The May-Hegglin/Fechtner Syndrome Consortium. *Nat Genet.* 2000;26(1):103-105.
4. Seri M, Pecci A, Di Bari F, et al. MYH9-related disease: May-Hegglin anomaly, Sebastian syndrome, Fechtner syndrome, and Epstein syndrome are not distinct entities but represent a variable expression of a single illness. *Medicine (Baltimore*). 2003;82(3):203-215.
5. Conti MA, Adelstein RS. Nonmuscle myosin II moves in new directions. *J Cell Sci.* 2008;121(Pt 1):11-18.
6. Niederman R, Pollard TD. Human platelet myosin, II: in vitro assembly and structure of myosin filaments. *J Cell Biol.* 1975;67(1):72-92.
7. Vicente-Manzanares M, Ma X, Adelstein RS, Horwitz AR. Non-muscle myosin II takes centre stage in cell adhesion and migration. *Nat Rev Mol Cell Biol.* 2009;10(11):778-790.
8. Kunishima S, Saito H. Advances in the understanding of MYH9 disorders. *Curr Opin Hematol.* 2010;17(5):405-410.
9. Murakami N, Mehta P, Elzinga M. Studies on the distribution of cellular myosin with antibodies to

isoform-specific synthetic peptides. *FEBS Lett.* 1991;288(1-2):247.

10. Balduini CL, Pecci A, Savoia A. Recent advances in the understanding and management of MYH9-related inherited thrombocytopenias. *Br J Haematol.* 2011;154(2):161-174.
11. Hu A, Wang F, Sellers JR. Mutations in human nonmuscle myosin IIA found in patients with May-Hegglin anomaly and Fechtner syndrome result in impaired enzymatic function. *J Biol Chem.* 2002;277(48):46512-46517.
12. Franke JD, Dong F, Rickoll WL, Kelley MJ, Kiehart DP. Rod mutations associated with MYH9-related disorders disrupt nonmuscle myosin-IIA assembly. *Blood.* 2005;105(1):161-169.
13. Adams DJ, Quail MA, Cox T, et al. A genome-wide, end-sequenced 129Sv BAC library resource for targeting vector construction. *Genomics.* 2005;86(6):753-758.
14. Jacobelli J, Friedman RS, Conti MA, et al. Confinement-optimized three-dimensional T cell amoeboid motility is modulated via myosin IIA-regulated adhesions. *Nat Immunol.* 2010;11(10):953-961.
15. Moeller MJ, Sanden SK, Soofi A, Wiggins RC, Holzman LB. Podocyte-specific expression of cre recombinase in transgenic mice. *Genesis.* 2003;35(1):39-42.
16. Takaku T, Malide D, Chen J, Calado RT, Kajigaya S, Young NS. Hematopoiesis in 3 dimensions: human and murine bone marrow architecture visualized by confocal microscopy. *Blood.* 2010;116(15):e41-e55.
17. Szabova L, Son MY, Shi J, et al. Membrane-type MMPs are indispensable for placental labyrinth formation and development. *Blood.* 2010;116(25):5752-5761.
18. Italiano JE Jr, Lecine P, Shivdasani RA, Hartwig JH. Blood platelets are assembled principally at the ends of proplatelet processes produced by differentiated megakaryocytes. *J Cell Biol.* 1999;147(6):1299-1312.
19. Thon JN, Montalvo A, Patel-Hett S, et al. Cytoskeletal mechanics of proplatelet maturation and platelet release. *J Cell Biol.* 2010;191(4):861-874.
20. Thon JN, Italiano JE. Platelet formation. *Semin Hematol.* 2010;47(3):220-226.
21. Junt T, Schulze H, Chen Z, et al. Dynamic visualization of thrombopoiesis within bone marrow. *Science.* 2007;317(5845):1767-1770.
22. Pecci A, Noris P, Invernizzi R, et al. Immunocytochemistry for the heavy chain of the non-muscle myosin IIA as a diagnostic tool for MYH9-related disorders. *Br J Haematol.* 2002;117(1):164-167.
23. Kopp JB. Glomerular pathology in autosomal dominant MYH9 spectrum disorders: what are the clues telling us about disease mechanism? *Kidney Int.* 2010;78(2):130-133.
24. Sekine T, Konno M, Sasaki S, et al. Patients with Epstein-Fechtner syndromes owing to MYH9 R702 mutations develop progressive proteinuric renal disease. *Kidney Int.* 2010;78(2):207-214.
25. Eckly A, Strassel C, Freund M, et al. Abnormal megakaryocyte morphology and proplatelet formation in mice with megakaryocyte-restricted MYH9 inactivation. *Blood.* 2009;113(14):3182-3189.
26. Chang Y, Aurade F, Larbret F, et al. Proplatelet formation is regulated by the Rho/ROCK pathway. *Blood.* 2007;109(10):4229-4236.
27. Chen Z, Naveiras O, Balduini A, et al. The May-Hegglin anomaly gene MYH9 is a negative regulator of platelet biogenesis modulated by the Rho-ROCK pathway. *Blood.* 2007;110(1):171-179.
28. Leon C, Eckly A, Hechler B, et al. Megakaryocyte-restricted MYH9 inactivation dramatically affects hemostasis while preserving platelet aggregation and secretion. *Blood.* 2007;110(9):3183-3191.
29. Ma X, Bao J, Adelstein RS. Loss of cell adhesion causes hydrocephalus in nonmuscle myosin II-B-ablated and mutated mice. *Mol Biol Cell.* 2007;18(6):2305-2312.
30. Johnstone DB, Zhang J, George B, et al. Podocyte-specific deletion of Myh9 encoding nonmuscle myosin heavy chain 2A predisposes mice to glomerulopathy. *Mol Cell Biol.* 2011;31(10):2162-2170.
31. Ma LJ, Fogo AB. Model of robust induction of glomerulosclerosis in mice: importance of genetic background. *Kidney Int.* 2003;64(1):350-355.
32. Barisoni L, Schnaper HW, Kopp JB. Advances in the biology and genetics of the podocytopathies: implications for diagnosis and therapy. *Arch Pathol Lab Med.* 2009;133(2):201-216.
33. Conti MA, Even-Ram S, Liu C, Yamada KM, Adelstein RS. Defects in cell adhesion and the visceral endoderm following ablation of nonmuscle myosin heavy chain II-A in mice. *J Biol Chem.* 2004;279(40):41263-41266.
34. Matsushita T, Hayashi H, Kunishima S, et al. Targeted disruption of mouse ortholog of the human MYH9 responsible for macrothrombocytopenia with different organ involvement: hematological, nephrological, and otological studies of heterozygous KO mice. *Biochem Biophys Res Commun.* 2004;325(4):1163-1171.
35. Poopak B, Rezvani H, Difeo A, et al. The first report of homozygous May-Hegglin anomaly E1841K mutation. *Eur J Haematol.* 2011;86(4):357.